High-harmonic generation in graphene: Interband response and the harmonic cutoff

Larisa A. Chizhova, Florian Libisch,* and Joachim Burgdörfer
Institute for Theoretical Physics, Vienna University of Technology (TUW), Wiedner Hauptstraße 8-10, 1040 Vienna, Austria, EU
(Received 25 July 2016; revised manuscript received 14 December 2016; published 27 February 2017)

We numerically examine the high-harmonic generation in graphene caused by an intense few-cycle terahertz laser field by solving the time-dependent Dirac equation. The observed spectra feature a complex interplay of interband and intraband electron dynamics. At high harmonic frequencies, we observe a plateau region with a cut-off frequency linearly proportional to the laser field. The linear dependence of the cutoff on the field resembles the behavior for electrons driven in bulk crystals but differs from the case of atoms or molecules. The unique features of the graphene band structure allow for a transparent decomposition of interband and intraband contributions and for an analytic estimate of the harmonic cut-off frequency in excellent agreement with the simulations.

DOI: 10.1103/PhysRevB.95.085436

I. INTRODUCTION

High-harmonic generation (HHG) in media interacting with strong laser pulses is an important aspect of nonlinear optics first discovered in gases [1,2]. In strong femtosecond laser fields an electron is liberated from an atom or molecule via above-threshold ionization (ATI) and recombines with the ionic core as the field reverses, emitting high-frequency photons [3]. The periodic sequence of driven emission and coherent radiative recombination in the laser field creates a train of bursts of HHG radiation with attosecond duration. The harmonic spectra of such a pulse train reveals a sharp cutoff [1,2], which scales linearly with the laser intensity I or quadratically with the laser field amplitude F_0, $I \approx F_0^2$.

The situation qualitatively changes in bulk semiconductors or dielectrics: recent studies of solid crystals (in ZnO [4], GaSe [5], and SiO_2 [6]) subject to intense laser pulses revealed high-harmonic generation with a cut-off energy scaling linearly with the laser field $\sim F_0$, i.e., with the square root of the laser intensity. Pronounced differences in the behavior of gases and solids sparked lively debates as to their origin [5–10].

Within a single-band model [4,6,11] the appearance of HHG in semiconductors was attributed to the nonlinear *intraband* response, in particular to Bragg reflections of the driven electrons at the Brillouin zone boundary, giving rise to so-called Bloch oscillations. Within this model the cut-off energy $U_c = \hbar\omega_c$ of the broadband HHG spectra is predicted to be proportional to the Bloch oscillation frequency $\omega_c \sim \Omega_B = |e|aF_0/\hbar$, where a is the lattice constant, for electrons reaching the zone boundary. The same scaling behavior of U_c was derived within a two-band model in the strong field limit [12]. In this case, the high frequencies are generated due to the transitions between Wannier-Stark states separated by multiples of $\hbar\Omega_B$, and not by the intraband response. However, this model fails to predict the harmonic generation of odd multiples of the driving field frequency ω in the spectra observed in various experiments. More involved approaches to HHG in solids considering multiple bands [7–10] anticipate that the HHG is governed not only by the anharmonic electron motion within one conduction band but by a complex interplay between the *intraband* and the *interband* responses. In particular, the interband polarization is predicted to dominate the high-energy part of the spectrum and the harmonic cutoff [8,9]. On the other hand, modeling the experimental high-harmonic spectrum in SiO_2 suggested the pivotal role of intraband dynamics [6]. The sensitive dependence of the intraband harmonic yield on the curvature of the band structure was proposed as a key ingredient for an all-optical probe of the band structure [13,14].

The number of proposed competing models underlines that the exact role of interband and intraband contributions for the solid state is still a widely open question. One source of ambiguity is the complicated band structures of the bulk materials considered so far. In the present work we therefore consider the conceptually much simpler system of a truly two-dimensional solid, graphene. This semimetal features a gapless spectrum, in contrast to the wide-band-gap bulk semiconductors previously studied experimentally [4,6,11] and theoretically so far [7–10,12–14]. The energy dispersion of electrons in graphene near the Fermi energy can be well approximated by a double Dirac cone. Bragg reflections at the Brillouin zone boundary are absent for low-energy excitations. In order to spectrally confine the emitted radiation to the region of a conelike band structure, we consider a few-cycle terahertz driving field with mean carrier energy (frequency) $\hbar\omega = 8$ meV ($\approx$2 THz). Harmonics up to the order n of about 100 still lie within the spectral region of the Dirac double cone. The present investigation is motivated not only by the goal to explore the nonlinear response of this two-dimensional solid currently investigated experimentally [15–20], but also to provide additional insights into the high-harmonic generation in condensed matter for an electronic structure fundamentally different from that of bulk semiconductors or dielectrics.

The source of a strong nonlinear response of electrons and holes in graphene is related to the near-linear energy dispersion close to the Dirac point [21,22]. Indeed, field-induced Zener-type electron transfer yields a strongly nonadiabatic behavior [23,24]. Here, we specifically investigate the HHG from graphene subjected to a short terahertz laser pulse, including effects of deviation from the perfect cone ("trigonal warping") and dephasing of interband coherence. Our calculations reveal HHG spectra with a broad harmonic plateau and a sharp energy cutoff. For the value of the cut-off energy determined by

*florian.libisch@tuwien.ac.at

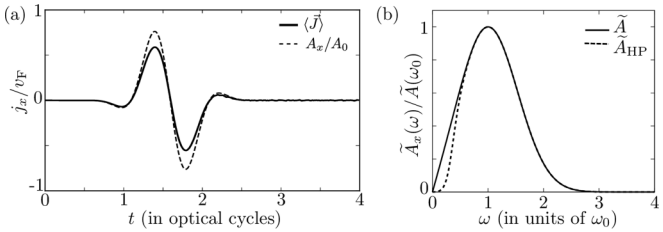

FIG. 1. (a) Calculated current (black curve) produced by electrons in graphene driven by a near-single-cycle 2-THz Gaussian envelope laser pulse of 40 kV/cm electric field strength (the black dashed curve shows its normalized vector potential). (b) Fourier transform of the vector potential in (a), (solid line) and after filtering out low-frequency components by a high-pass (HP) filter (dashed line).

interband polarization an analytical estimate can be given in good agreement with numerical simulations, scaling linearly with the field strength of the driving terahertz field.

The present paper is organized as follows: In Sec. II we briefly review the methods employed for analyzing the nonlinear response of graphene. Simulation results for ideal graphene as well as for the influence of dephasing and doping are presented in Sec. III, followed by concluding remarks in Sec. IV.

II. METHODS

We theoretically examine the response of graphene to short terahertz (THz) laser pulses, described by a vector potential $\vec{A}(t)$, by solving the time-dependent Dirac equation (TDDE)

$$i\hbar\frac{\partial}{\partial t}|\psi(t)\rangle = v_F(\vec{p} + |e|\vec{A}(t))\cdot\hat{\vec{\sigma}}|\psi(t)\rangle, \tag{1}$$

where $v_F = 10^6$ m/s is the Fermi velocity, $\hat{\vec{\sigma}} = (\hat{\sigma_x},\hat{\sigma_y})$ are the Pauli matrices, and $\vec{F}(t) = -\frac{d}{dt}\vec{A}(t)$ is the electric field of the pulse with peak field strength F_0. We treat the electromagnetic field in the velocity gauge, which eliminates the electric field from the Hamiltonian. While this gauge avoids numerical difficulties associated with the large r behavior of the electron-pulse interaction ($\approx \vec{r}\cdot\vec{F}$) in real space, it may face divergence problems in the (near) static limit ($\omega \to 0$) [24,25], as this limit corresponds to an ever-increasing vector potential $\vec{A}(t)$. In the present case, however, the near-zero frequency contributions of the driving field $\vec{A}(\omega \approx 0)$ to high-harmonic generation can be safely neglected. The influence of such a spurious contribution can be directly controlled by applying a high-pass (HP) filter to the Fourier amplitude $\tilde{F}(\omega)$ of the original few-cycle driving pulse $F(t)$, thereby assuring vanishing low-frequency contributions in $\tilde{F}_{HP}(\omega)$ in the vicinity of $\omega = 0$. Solving Eq. (1) with the corresponding vector potential $A_{HP}(t)$ [see dashed line in Fig. 1(b)] yields an essentially unchanged harmonic spectrum compared to the original pulse, verifying that the HHG remains unaffected by spurious low-frequency contributions.

We determine the one-particle density matrix $\rho(t)$ by propagating its eigenstates, the natural orbitals, according to Eq. (1),

$$\rho(t) = \sum_j P_j|\psi_j(t)\rangle\langle\psi_j(t)|, \tag{2}$$

where P_j are the occupation numbers prior to the arrival of the pulse ($t \to -\infty$) described by a Fermi-Dirac distribution

$$P_j = f_{FD}(E_j - \mu, T). \tag{3}$$

We refer to the time-evolved natural orbitals $|\psi_j(t)\rangle$ as quantum trajectories. At $t \to -\infty$ the initial states with well-defined momentum $\vec{p}$ and energy $E_\xi = \xi v_F|\vec{p}|$ are the solutions of the stationary Dirac equation:

$$\psi_{\vec{p}}^{\xi} = \frac{1}{\sqrt{2}}\begin{pmatrix} e^{-i\theta_{\vec{p}}/2} \\ \xi e^{i\theta_{\vec{p}}/2}\end{pmatrix}. \tag{4}$$

Here $\xi = \pm 1$ is the (conduction/valence) band index and $\theta_{\vec{p}}$ is the directional angle of the electron momentum, i.e., $\theta_{\vec{p}} = \arctan(p_y/p_x)$. Driven by the electric field of the laser such a quantum trajectory moves along the Dirac cone. Restricting the motion to a single band, the state would change its energy as

$$E_\xi(t) = \xi v_F|\vec{p} + |e|\vec{A}(t)|. \tag{5}$$

Within the two-band model of the Dirac double cone, a state can be partially transferred to the upper cone by Landau-Zener–type interband tunneling [26] if the initial momentum component orthogonal to the laser polarization direction, assuming linear polarization of the laser, is nonzero. For vanishing transverse momentum, the trajectory passes through the Dirac point and can undergo complete population inversion [21,23,27]. The tunneling mechanism induces an interband polarization by splitting the quantum trajectory into two paths coherently propagating on the upper and the lower cones. This interband polarization is expected to crucially influence the high-harmonic spectrum. The single-particle current density $\vec{j}_{\vec{p}}^{\xi}$ associated with a given quantum trajectory with initial momentum $\vec{p}$ started from a band with index ξ can be evaluated as

$$\vec{j}_{\vec{p}}^{\xi}(t) = \langle\psi_{\vec{p}}^{\xi}(t)|\hat{\vec{j}}|\psi_{\vec{p}}^{\xi}(t)\rangle = v_F\langle\psi_{\vec{p}}^{\xi}(t)|(\hat{\sigma}_x,\hat{\sigma}_y)|\psi_{\vec{p}}^{\xi}(t)\rangle, \tag{6}$$

where $\hat{\vec{j}}$ denotes the current operator, which in the case of Dirac particles is proportional to Pauli matrices $\hat{\sigma}_{x,y}$.

Following Ref. [21], the Dirac equation for a quantum trajectory [Eq. (1)] can be conveniently rewritten in terms of optical Bloch-type equations, which allows for a straightforward generalization in the presence of scattering and dephasing as discussed below. Accordingly, we expand the time-dependent wave function on the double cone as

$$\psi(t) = \sum_{\xi=\pm1} C_\xi(t)\psi_\xi(t), \tag{7}$$

where the wave function within each band $\psi_\xi(t)$ changes according to

$$\psi_\xi(t) = \frac{1}{\sqrt{2}}\begin{pmatrix} e^{-i\theta_{\vec{n}}(t)/2} \\ \xi e^{i\theta_{\vec{n}}(t)/2}\end{pmatrix}\exp(-i\phi_\xi(t)), \tag{8}$$

with the temporal phase

$$\phi_\xi(t) = \frac{1}{\hbar}\int_0^t E_\xi(t')dt' = \xi\frac{v_F}{\hbar}\int_0^t |\vec{p} + |e|\vec{A}(t')|dt'. \quad (9)$$

Here $E_\xi(t')$ describes time-dependent energy of the particle driven by an external field [Eq. (5)]. During the time propagation the directional angle changes as

$$\theta_{\vec{\Pi}}(t) = \arctan\left(\frac{p_y + |e|A_y(t)}{p_x + |e|A_x(t)}\right), \quad (10)$$

where $\vec{\Pi} = \vec{p} + |e|\vec{A}(t)$ is the kinematic momentum. Substituting the wave-function expansion Eq. (7) into the TDDE [Eq. (1)] results in a system of differential equations for the expansion coefficients $C_\xi(t)$, which can be rewritten in the form of optical Bloch equations

$$\begin{aligned}
\dot{\zeta}(t) &= -\frac{i}{2}\dot{\theta}_{\vec{\Pi}}(t)[\eta_c(t) - \eta_v(t)]e^{2i\phi(t)},\\
\dot{\eta}_c(t) &= -\frac{i}{2}\dot{\theta}_{\vec{\Pi}}(t)\zeta(t)e^{-2i\phi(t)} + \text{c.c.},\\
\dot{\eta}_v(t) &= \frac{i}{2}\dot{\theta}_{\vec{\Pi}}(t)\zeta(t)e^{-2i\phi(t)} + \text{c.c.},
\end{aligned} \quad (11)$$

after introducing conduction ($\eta_c = |C_+|^2$) and valence ($\eta_v = |C_-|^2$) band occupation probabilities and the interband coherence $\zeta = C_+C_-^*$. The single-electron current density can now be expressed as [21]

$$\begin{aligned}
j_{\vec{p},x}(t) &= v_F[(\eta_c - \eta_v)\cos(\theta_{\vec{\Pi}})\\
&\quad + i(\zeta e^{-2i\phi} - \zeta^* e^{2i\phi})\sin(\theta_{\vec{\Pi}})], \quad (12a)\\
j_{\vec{p},y}(t) &= v_F[(\eta_c - \eta_v)\sin(\theta_{\vec{\Pi}})\\
&\quad - i(\zeta e^{-2i\phi} - \zeta^* e^{2i\phi})\cos(\theta_{\vec{\Pi}})]. \quad (12b)
\end{aligned}$$

The current generated by a particle moving within one band with band index ξ, i.e., the intraband current, is

$$\begin{aligned}
j^\xi_{\vec{p},x}(t) &= \xi v_F\cos(\theta_{\vec{\Pi}}),\\
j^\xi_{\vec{p},y}(t) &= \xi v_F\sin(\theta_{\vec{\Pi}}).
\end{aligned} \quad (13)$$

Comparison between Eqs. (12) and (13) shows that the current density [Eqs. (12)] contains both an intraband contribution [first terms in Eqs. (12a) and (12b)] and an interband polarization contribution [second terms in Eqs. (12a) and (12b)].

The total current determining the response of graphene to a THz pulse is given by the ensemble average of single-electron currents $\vec{j}^\xi_{\vec{p}}(t)$ [Eq. (6) or Eq. (12)] generated by the time evolution of initially occupied states:

$$\langle\vec{J}\rangle = \frac{4}{(2\pi\hbar)^2}\sum_\xi\int d^2p\cdot\vec{j}^\xi_{\vec{p}}(t)\cdot f_{\text{FD}}(\xi v_F|\vec{p}| - \mu, T). \quad (14)$$

Here, the factor of 4 results from the spin and the valley degeneracies. Note that the integral in Eq. (14) extends over all Bloch states with initial momenta weighted by their initial occupation given by f_{FD}.

As we verified numerically, the effect of finite temperature (up to room temperature) and finite doping ($\mu \neq 0$, where the energy of the Dirac point is set to zero) on the high-harmonic spectrum is weak as long as the respective energy scales are small compared to the ponderomotive energy [3,28]. The latter is defined as the average quiver energy of the oscillating electron in the laser field, $U_p = F_0^2/(4m\omega^2)$. We therefore average over electrons initially occupying at $t \to -\infty$ the valence band ($\mu = 0$) with initial energies $E_{\text{min}} \leqslant E \leqslant 0$ eV at $T = 0$. E_{min} is the minimum energy of a state in the valence band that can be driven up to the Dirac point by the strong THz pulse. Since lower-lying initial states do not reach the Dirac point during the time evolution of the pulse they will not significantly contribute to the high-harmonic part of the spectra. We have numerically verified that HHG does not depend on the precise numerical value of E_{min}. An example of the calculated electron response of graphene, i.e., $\langle\vec{J}\rangle$, to a 2-THz pulse with a Gaussian envelope of pulse duration $t_p = 250$ fs and field strength of 40 kV/cm is displayed in Fig. 1. Using the field $A_{\text{HP}}(t)$ following from inverse Fourier transform of the high-pass filtered signal instead of the unfiltered $A(t)$ yields the same $\langle\vec{J}\rangle$ within graphical accuracy.

Alternatively to the Dirac equation continuum model Eq. (1), the nonlinear response can also be calculated within the framework of a tight-binding approach by solving the time-dependent Schrödinger equation for a tight-binding (TDTB) Hamiltonian applied to finite-sized flakes [27]. The total current determining the response

$$\langle\vec{J}\rangle = 2\sum_n \vec{j}_n(t)\cdot f_{\text{FD}}(\epsilon_n) \quad (15)$$

is calculated as an ensemble average over single-electron currents $\vec{j}_n$ determined by the time evolution of occupied eigenstates $|\psi_n\rangle$ (with eigenenergies ϵ_n) of a rectangular graphene flake with periodic boundary conditions along the laser pulse, i.e., along the x direction. We screen the zigzag edges parallel to the x axis by applying a Berry-Mondragon potential to suppress strong edge localization effects [29]. Unlike the TDDE, this approach accounts for the hexagonal lattice structure from the outset. However, it contains finite-size effects of the flake. A numerical comparison between the two methods is presented below.

The far-field response generated by the induced currents in graphene under the influence of the laser field is given by the dipole acceleration. The spectral power of the far field can be evaluated from the Fourier transform of the dipole acceleration or, equivalently, from the Fourier transform of the total current as

$$P(\omega) \sim |\ddot{\vec{d}}(\omega)|^2 \sim |\omega\vec{J}(\omega)|^2. \quad (16)$$

We evaluate Eq. (16) for graphene driven by few-cycle THz pulses with a well-defined carrier-envelope phase (CEP). In the following we always show the spectral power normalized to the intensity of the first harmonic, the fundamental of the driving field.

III. SIMULATIONS

A. Ideal graphene

We consider in the following the response of graphene to a linearly polarized THz pulse along the x axis given by the

vector potential

$$A(t) = A_0 \sin(\omega t + \phi_{CEP}) e^{-\frac{t^2}{2t_p^2}} \tag{17}$$

with amplitude A_0, a Gaussian envelope with pulse duration $t_p = 250$ fs, and CEP phase ϕ_{CEP}. Such a sinelike vector potential corresponds to an approximatively cosinelike shape of the electric field of the pulse. We choose the pulse frequency $\omega = 2\pi\nu$ with $\nu = 2$ THz and a peak field amplitude corresponding to $F_0 = \omega A_0 = 40$ kV/cm. Since the ideal double Dirac cone is rotationally invariant, the direction of the polarization axis is irrelevant. This, however, will change when trigonal warping, i.e., the deformation of the cone due to the underlining hexagonal lattice structure, is taken into account as discussed below.

In this section we evaluate the response of graphene by explicitly solving the time-dependent Dirac equation [Eq. (1)] with initial conditions given by Eq. (4) and by summing over the occupied stated in the $\vec{k}$ space [Eq. (14)]. We can then directly calculate the current density using Eq. (6). A typical current response to a near single-cycle pulse with $\phi_{\text{CEP}} = 0$ results in a high-harmonic spectrum [see Figs. 2(a)–2(c)] consisting of three main regions: (i) a dominant part of low-frequency harmonics exponentially decaying as a function of E; (ii) an extended plateau region; and (iii) a sharp cutoff at high frequencies. Qualitatively similar spectra were first observed for laser-irradiated gases [1,2]. The generation of high-frequency photons in gases can be intuitively explained by a three-step model: the electron liberated from the atom by tunneling ionization gets accelerated by the laser field and eventually returns to the ionic core, where it radiatively recombines, emitting a high-frequency photon. Correspondingly, the atomic cut-off energy U_c^a is given by the maximum kinetic energy gain after which an electron can still return back to its core and is classically estimated as [3]

$$U_c^a = I_p + 3.17U_p = I_p + 3.17e^2F_0^2/4m\omega^2, \tag{18}$$

where I_p is the ionization potential of the atom and $U_p = F_0^2/(4m\omega^2)$ the ponderomotive energy [3,28]. Equation (18) scales with the square of the peak field strength $\sim F_0^2$ or, more precisely, of the vector potential $\sim A_0^2 \approx (F_0/\omega)^2$.

A corresponding simple picture for harmonic generation by the electronic motion in the periodic crystal potential is still a matter of debate. The present case of graphene may provide important insight along those lines. The natural starting point for condensed-matter harmonics is the (quasi-) momentum rather than a real-space picture (Fig. 3). In order to explore the origin of the harmonics, we first perform a windowed Fourier transform (WFT) [30] of the current. In Figs. 2(a)–2(c) (bottom panels) we observe two major bursts of harmonic radiation. The first one, when the vector potential reaches its first maximum $A_{\max}$, includes radiation up to energies $\sim 0.5\, U_c^g$, while the second burst emitted near the following extremum $A_{\min}$ reaches all the way up to the cut-off energy for graphene, U_c^g. For the remaining laser pulse the spectrum remains confined to energies below $\lesssim 0.5\, U_c^g$. The appearance of high harmonics within a narrow time window and their energy cutoff can be understood as follows. Consider an electron with initial electron momentum $p_x^0 \approx -|e|A_0$ ($p_y \ll p_x$) and energy $E_0 \approx -v_F|e|A_0$ [Fig. 3(a) at t_0]. $|E_0|$ coincides with the

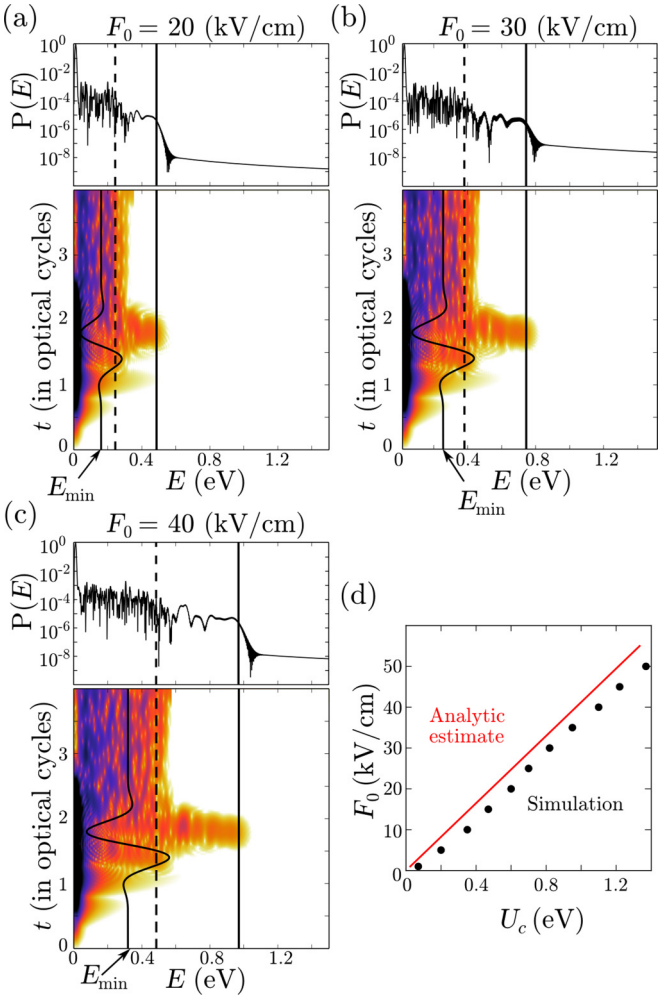

FIG. 2. (a)–(c) Integrated (top frame) and time-resolved (bottom frame) spectral power $P(E)$ of the far-field response of the graphene to a 2-THz, one-cycle Gaussian laser pulse with zero carrier-envelope phase and duration $t_p = 250$ fs. We normalize the spectral power to the intensity of the first harmonic. The peak amplitudes of the laser field are (a) $F_0 = 20$ kV/cm, (b) $F_0 = 30$ kV/cm, and (c) $F_0 = 40$ kV/cm. We use the linear dispersion relation $E(t) = v_F|e|A(t)$ of Dirac fermions with $v_F = 10^6$ m/s (shown as black curve in bottom frame starting with $E(0)$ at the minimum energy $|E_{\min}| = v_F|e|A_0$). Solid vertical lines show the theoretically estimated harmonic cutoff U_c^g. Dashed vertical lines correspond to $0.5\, U_c^g$. (d) Theoretically estimated (red line, $v_F^0 = 0.78 \times 10^6$ m/s) and computed (black dots) harmonic cutoffs as a function of the laser field strength.

maximum energy a Dirac electron can pick up from the laser field. At the maximum of the vector potential this electron is brought close to the Dirac point $p_x = p_{x0} + |e|A_0 \approx 0$ [Fig. 3(a) at t_1]. E_0 therefore coincides with $E_{\min}$, the lowest energy of a state on the valence cone that can be driven up to the Dirac point by the pulse. Near the Dirac point the quantum trajectory splits into two components, one of which is excited to the conduction band by interband Landau-Zener tunneling [26], while the other remains in the valence band [see Fig. 3(c)]. The resulting superposition of the two wave packets results in high-frequency oscillations of the single-electron current $j_x(t)$. The oscillation frequency is determined

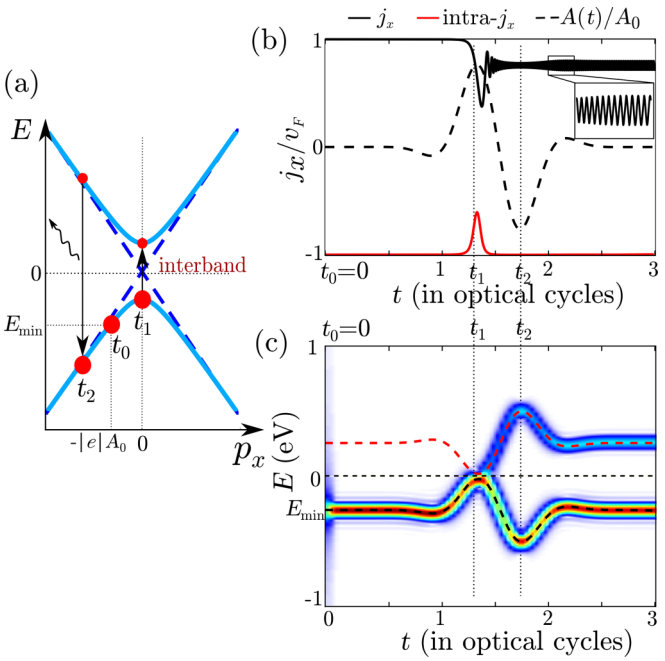

FIG. 3. (a) Schematic illustration of high-energy harmonic generation in graphene and of the harmonic cutoff. The depicted initial state contributes to the harmonic emission near the cutoff. At $t_0 \to -\infty$ the state has momentum $p_x \approx -|e|A_0$ ($p_y \ll p_x$) and energy $E_0 \approx -v_F|e|A_0$. At the maximum of the vector potential (at time t_1) the momentum of the electron is close to $p_x \approx 0$ and its energy reaches the Dirac point (with $p_y = \text{const}$), allowing for Landau-Zener tunneling between the two bands. The maximal energy distance between the two pieces of the split wave packet is reached at the following minimum of the vector potential (at time t_2) determining the cut-off energy of the harmonic radiation emitted upon electron-hole recombination. (b) Single-electron current (black curve) generated by a quantum trajectory $\psi(t)$ for an initial state (at $t \to -\infty$) with momentum $\vec{p} = (p_x, p_y) = (-0.8, 0.05)|e|A_0$ and an energy close to $E_{\min}$ evaluated by solving the TDDE [Eqs. (1) and (6)]. The intraband current (for a state moving within only one band) evaluated using Eq. (13) and multiplied by –1 for better visibility is shown in red. Black-dashed curve represents the vector potential of the pulse. (c) Windowed Fourier transform of the quantum trajectory $\psi(t)$ depicted in (a). Black and red dashed curves follow the energy evolution of a state within a single (valence/conduction) band, i.e., $E_\xi(t)$ [Eq. (5)].

by the derivative of the temporal phase difference between the two wave packets, $\Omega(t) = \Delta\dot{\phi}(t) = (E_+(t) - E_-(t))/\hbar = 2E_+(t)/\hbar$ [21]. For this particular quantum trajectory, the maximal possible phase velocity and, therefore, energy difference between the two (conduction and valence band) paths is achieved at the subsequent extremum of the vector potential [at t_2, with $A(t_2) = -A_0$, see Fig. 3(a)], determining the energy cutoff:

$$U_c^g = 2v_F|e|(A_{\max} - A_{\min}) \approx 4v_F|e|A_0 = 4v_F|e|F_0/\omega. \quad (19)$$

This cutoff is proportional to A_0 and depends not only on the field strength, but also on the inverse driving frequency similar to U_c^a [Eq. (18)]. This is qualitatively different from the radiation associated with Bloch oscillations. Our theoretical estimate of U_c^g [see solid black lines in Figs. 2(a)–2(c) and red line in Fig. 2(d)] agrees well with our simulations [see black dots in Fig. 2(d)]. The small deviation between theoretical estimate and calculations can be explained by tunneling of electrons with energies slightly below $E_{\min}$. The probability of such events, however, decays exponentially with increasing $|E|$.

To illustrate a typical quantum trajectory contributing to the spectrum near the harmonic cutoff, we solve the TDDE for an initial state with $\vec{p} = (-0.8, 0.05)eA_0$ and $E = -0.8v_F|e|A_0$. The windowed Fourier transform of $\psi(t)$ traces the energy evolution $E(t)$ of the state [Fig. 3(c)]. Upon reaching the Dirac point at $t \approx t_1$, the initial wave packet splits into two. These two pieces of the wave packet gain the largest phase difference at the minimum of the vector potential, $t \approx t_2$. Moreover, the single-electron current [black curve in Fig. 3(b)], evaluated by Eq. (6), reveals rapid oscillations. These oscillations are present only after the split of the trajectory due to tunneling near the Dirac point, i.e., at times $t \gtrsim t_1$ [see Fig. 3(c)]. There is an obvious correlation between the frequency of these oscillations and the energy difference between the two pieces of the wave packet propagating in the valence and conduction bands. The highest frequency is found when the phase difference between the two wave packets [or the energy difference between the two trajectories $E_\xi(t)$] is maximal. The intraband current [red curve in Fig. 3(b)] calculated for an electron moving only within the valence band using Eq. (13) does not show such oscillations. It coincides with the total current [black curve in Fig. 3(b)] only at the beginning of the pulse, i.e., $t \lesssim t_1$, when the electron moves only within the valence band. One noteworthy point of conceptual interest is that Bragg reflections are entirely absent from the dynamics on the Dirac double cone. Therefore, Bloch oscillations do not significantly contribute to the harmonic generation in graphene. The (mostly) low-order intraband harmonic contribution probes the curvature of the valence band near the Dirac point (for $p_y \ll p_x$).

In the time-resolved Fourier spectrum we observe a second lower cutoff effective after the pulse has concluded [marked by dashed vertical lines in Figs. 2(a)–2(c)]. This cutoff originates from the residual interband polarization. The maximum oscillation frequency in the single-electron current in this regime is governed by the same trajectories (in energy space) also responsible for the main cutoff [Figs. 3(b) and 3(c)]. After the pulse is over, the wave packet in the lower band returns to its initial state with energies near $-|E_{\min}| = -v_F|e|A_0$ and the wave packet in the upper band correspondingly returns to a state with $|E_{\min}|$. The frequency of the oscillations of the current produced by the superposition of these two states is $\Omega = (E_+ - E_-)/\hbar = 2|E_{\min}|/\hbar$, which results in a cutoff at $0.5\,U_c^g$.

We turn now to the many-electron response of a graphene sheet with $\mu = 0$, i.e., a completely occupied valence cone at $T = 0$ [Eq. (14)]. All electrons in the valence band occupying states with energies in the interval $E_{\min} \leqslant E \leqslant 0$ can reach the upper cone via Zener tunneling contributing to both intraband and interband polarization radiation. Indeed, valence electrons above $E_{\min}$ account for the dominant fraction of the total harmonic spectrum (see red trace in Fig. 4), and at high energies (up to the cut-off energy) their contribution

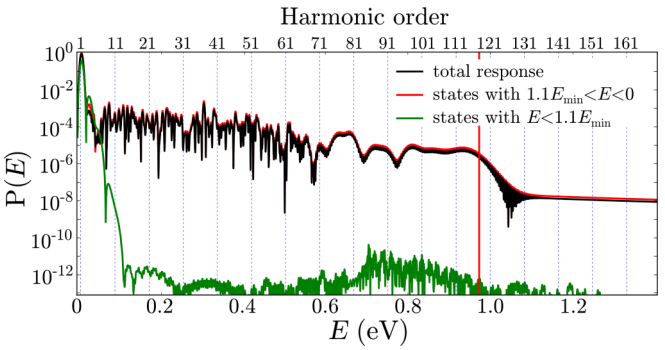

FIG. 4. High-harmonic generation in graphene. The total nonlinear response of graphene is shown in black; red trace corresponds to the response of electrons near the Dirac point with energies $1.1E_{\min} < E < 0$ contributing to the high-harmonic part of the spectra. The response of electrons further away from the Dirac point with $E < 1.1E_{\min}$ (green) contribute only to low-order harmonics.

coincides with the total response (see black trace in Fig. 4). By contrast, electrons with energies below $E_{\min}$ have an exponentially small tunneling probability between the two cones and hence contribute only to the intraband current. The integrated response of electrons with $E \lesssim E_{\min}$ (see green trace in Fig. 4) yields predominantly low harmonics stemming from the intraband current. Contributions to the plateau and the cut-off region are absent. It should be noted that this component of the intraband current does not probe the steep variations of the cone near the Dirac point.

While the carrier-envelope phase of the laser pulse does not influence the cut-off energy, it influences the shape of the high-energy tail. In particular, a pulse with a CEP of $\pi/2$ causes a strongly fluctuating pattern near the cutoff [Fig. 5(a)] as compared to the similar pulse with zero CEP [Fig. 2(b)]. Longer pulses, e.g., a ten-cycle pulse with a Gaussian envelope and with zero CEP [Fig. 5(b)], leave the cutoff [Eq. (19)]

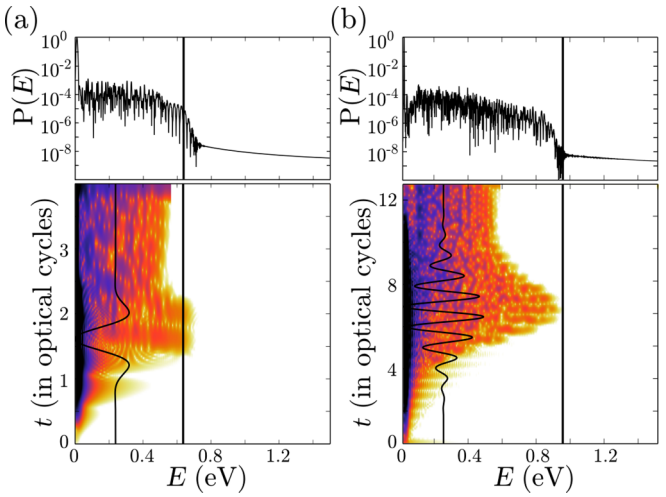

FIG. 5. High-harmonic spectra of graphene subject (a) to a 2-THz Gaussian laser pulse with duration $t_p = 250$ fs and carrier-envelope phase (CEP) of $\phi_{\text{CEP}} = \pi/2$; (b) to a 2-THz Gaussian laser pulse with duration $t_p = 1240$ fs (CEP = 0); in each case for a peak field strength of $F_0 = 30$ kV/cm.

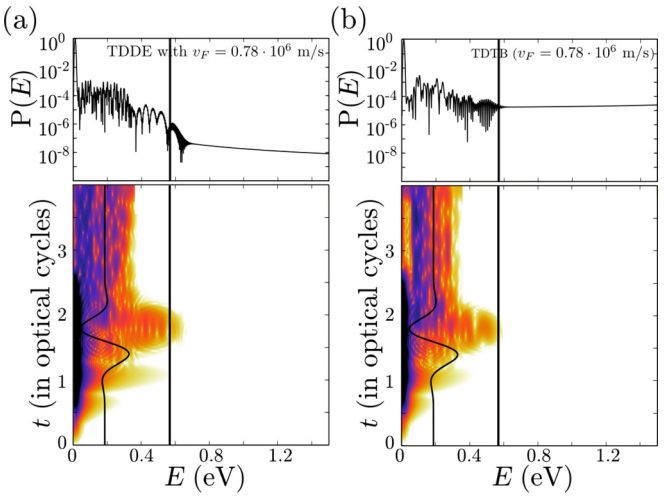

FIG. 6. Comparison between (a) the TDDE and (b) the TDTB for the same Gaussian 2-THz laser pulse ($\phi_{\text{CEP}} = 0$, $t_p = 250$ fs) with $F_0 = 30$ kV/cm calculated for identical Fermi velocity $v_F^0 = 0.78 \times 10^6$ m/s determined by our tight-binding parametrization. [Note the shift of the cutoff compared to that presented in Fig. 2(b).]

unchanged but result in a strongly fluctuating high-harmonic tail similar to that of a short pulse with CEP of $\pi/2$. In both cases this behavior near the cutoff can be attributed to intercycle interferences, i.e., the generation of high-energy trajectories within the different laser cycles. Since for a short laser pulse with zero CEP the high-energy trajectories contributing to the high-energy part of the spectra are generated only within one laser cycle, the high-energy tail of the spectra is smooth.

The harmonic cutoff U_c^g should depend linearly on the Fermi velocity v_F [Eq. (19)]. Our numerical results confirm this behavior: we evaluate the response of graphene by solving the TDDE and the TDTB for a different Fermi velocity of $v_F = 0.78 \cdot 10^6$ m/s [see Figs. 6(a) and 6(b)]. The HHG spectrum clearly displays the expected shift of the harmonic cutoff to the lower energy, in agreement with Eq. (19). [Compare to Fig. 2(b), where we evaluated the response within the TDDE approximation with $v_F = 10^6$ m/s.] The Fermi velocity chosen is given by the band structure resulting from our tight-binding parametrization [31]. Overall, the TDDE and TDTB results agree quite well [compare harmonic spectra in Figs. 6(a) and 6(b)]. Minor differences are due to finite-size effects and differences in the underlying band structure discussed in the following. The dependence of the cutoff on the Fermi velocity may provide a route towards determining v_F complementing standard angular resolved photoemission spectroscopy (ARPES) techniques. Since the dispersion relation is probed in a well-defined energy window determined by the pulse strength, Fermi velocity renormalizations close to the Dirac point [32] can be probed.

B. Effect of trigonal warping

The Dirac equation for massless fermions approximates the graphene band structure near the K and K' points only in the low-energy limit (up to $|E| \approx 0.2$ eV). At higher energies the rotationally symmetric double-cone band structure does

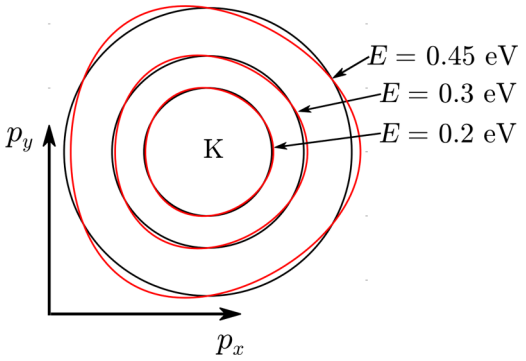

FIG. 7. Cross sections through an ideal Dirac cone (black) and a deformed Dirac cone with trigonal warping (red) taken at different energies: $E = 0.2$, 0.3, and 0.45 eV.

not account for the trigonal deformation of the circular cross section of the cones called trigonal warping. The TDTB method, including third-order tight-binding couplings, quantitatively accounts for this effect. Trigonal warping becomes important for pulses we consider here. For example, for a field strength of the pulse of 40 kV/cm, the critical energy, which Dirac fermions can gain from the laser field, is $E_{\min} = 0.31$ eV. At these energies the trigonal warping effect can no longer be neglected (Fig. 7). Within the Dirac double-cone model trigonal warping can be included by a correction term to the Dirac Hamiltonian [33]:

$$H^{\text{war}}(p) = -\mu\left[\left(p_x^2 - p_y^2\right)\cdot\hat{\sigma}_x - 2p_x p_y\hat{\sigma}_y\right], \qquad (20)$$

where $\mu \approx 5$ eV Å^2 is the trigonal warping coefficient. Analogously to the TDDE for the ideal Dirac cone, we calculate the time evolution of the single-electron wave function $\psi(t)$ for an initial state (at $t \to -\infty$) with a well-defined momentum $\vec{p}$. We start from the solution of the stationary Dirac equation with an additional warping potential $H^{\text{w}}(p)$,

$$\psi_\xi(\vec{p}) = \frac{1}{\sqrt{2}}\begin{pmatrix}\xi\cdot e^{i\arg[v_F e^{-i\theta_{\vec{p}}} - \mu p e^{2i\theta_{\vec{p}}}]}\\ 1\end{pmatrix}, \qquad (21)$$

and modified energy dispersion

$$E_\xi^{\text{w}} = \xi p\sqrt{v_F^2 + \mu^2 p^2 - 2v_F\mu p\cos(3\theta_{\vec{p}})}, \qquad (22)$$

where p is the absolute value of momentum.

The far-field response of graphene to a 2-THz pulse with Gaussian envelope ($t_p = 250$ fs) in the case of the warped Dirac cone becomes slightly modified (Fig. 8). In particular, for a pulse linearly polarized in x direction, the cutoff shifts to higher energies. This shift depends on the amount of trigonal warping, as it modifies the band structure and, therefore, the group velocity. Depending on the polarization direction of the pulse, the group velocity $v_g = \partial E/\partial k_x$ changes during the wave-packet propagation compared to the Fermi velocity of the unperturbed Dirac cone. For polarization in x direction and for initial states with $p_x < 0$ the group velocity increases ($v_g > v_F$). Therefore these states can gain more energy from the same pulse, resulting in a higher cut-off energy. The overall intensity of the HHG spectra, however, remains similar to the unperturbed case.

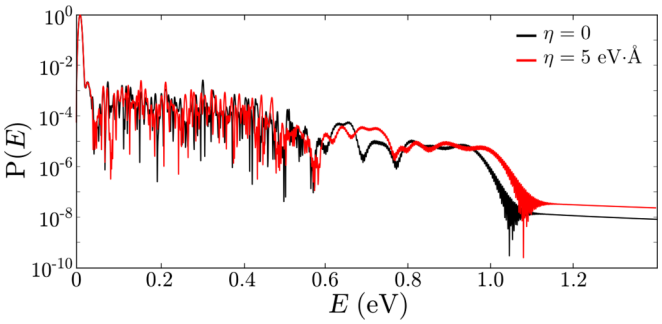

FIG. 8. The spectral power $P(E)$ of the far-field response of graphene to a Gaussian 2-THz laser pulse with duration $t_p = 250$ fs and field strength of 40 kV/cm calculated by TDDE with (red curve) and without (black curve) trigonal warping of the Dirac cone.

C. Effect of dephasing

The high-frequency contributions due to interband polarization result from the coherence between the two trajectories propagating within the conduction and valence bands. Therefore, the harmonic spectrum, in particular near the cutoff U_c^g, is expected to be sensitive to dephasing and decoherence. Electron-electron or electron-phonon scattering may lead to a loss of coherence and hence to the decay of oscillations. Typical decoherence times due to electron-phonon scattering are estimated to be of the order of picoseconds [34,35]. For high-energy excitations (∼1.2 eV) strongly inelastic electron-electron scattering times are of an order of 50 fs; for lower energies they are considerably larger [36]. We simulate the decay of interband polarizations within the relaxation-time approximation by introducing a dephasing time T_2, giving rise to a dephasing term proportional to $1/T_2$ in the optical Bloch equation for ζ [Eq. (11)] [8,9]:

$$\dot{\zeta}(t) = -\frac{\zeta}{T_2} - \frac{i}{2}\dot{\theta}_{\vec{\Pi}}(t)[\eta_c(t) - \eta_v(t)]e^{2i\phi(t)}. \qquad (23)$$

Absence of dephasing corresponds to $T_2 = \infty$, and a dephasing time $T_2 = 500$ fs is chosen to match the cycle period of the pulse. Based on the time scales available in the literature [34–36], we choose $T_2 = 80$ fs as an estimate for a small

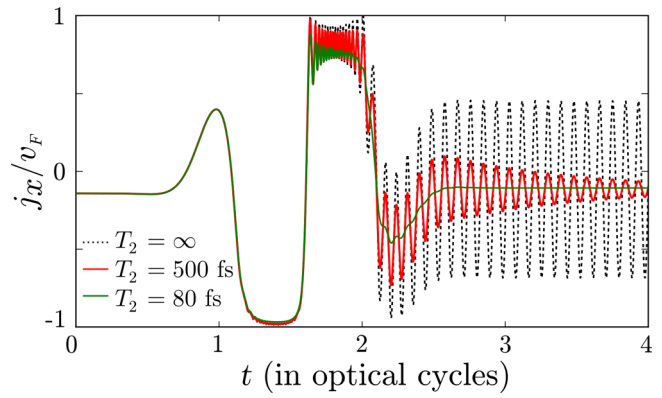

FIG. 9. An example of single-electron current $\vec{j}(t)$ calculated by optical Bloch equations with different dephasing times: $T_d = \infty$ (black dashed curve), i.e., no dephasing; $T_d = 500$ fs (red curve), i.e., T_d is equal to the period of the pulse; and $T_d = 80$ fs (green curve).

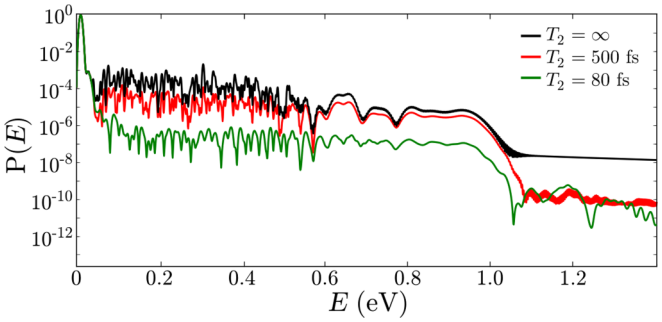

FIG. 10. The spectral power $P(E)$ of the far-field response of graphene at $T = 0$ to a Gaussian 2-THz laser pulse with duration $t_p = 250$ fs and peak field strength of 40 kV/cm calculated by optical Bloch equations with different dephasing times: $T_2 = \infty$ (black curve); $T_2 = 500$ fs (red curve); and $T_2 = 80$ fs (green curve).

dephasing time. As expected, the high-frequency components are monotonically damped with decreasing T_2 (Fig. 9). Only the low-harmonic portion remains unaffected by T_2.

The power spectrum $P(E)$ of the total current $\langle \vec{J}(t) \rangle$ (Fig. 10) for the ensemble of valence band electrons [Eq. (14)] displays a reduction of the HHG spectrum with decreasing T_2. At the same time, the noisy fluctuations in $P(E)$ are reduced in favor of equispaced harmonics. Similar results have been found in two-band model simulations for semiconductors [8,9]. This is a direct consequence of the decay of interband coherence. As a result the intraband response of incoherent charge motion within either conduction or valence bands becomes more important in the presence of decoherence in the system.

IV. CONCLUSION

High-harmonic generation in graphene is the result of an interplay between intraband and interband contributions. The simplicity of the band structure well approximated by the Dirac double cone allows for a transparent decomposition of the mechanisms underlying harmonic radiation. While the low harmonic orders (i.e., the third- and fifth-order harmonics) are predominantly caused by the intraband current near the Dirac point, the high-energy portion close to the cutoff is exclusively due to interband polarization. The cut-off energy can be analytically determined from the interference of two quantum paths propagating in the valence and conduction bands prior to recombination. The interference term contains oscillations in the current with frequencies determined by the energy difference between the two paths. These oscillations are very sensitive to the amount of dephasing in the system. The highest frequency of the oscillations produces the energy cutoff U_c^g, which is proportional to the vector potential of the laser field or, more precisely, to the difference between maxima and minima of the vector potential for short pulses. Notably, our estimate of the cut-off energy U_c^g does not depend on the carrier-envelope phase and is applicable to any shape of the pulse. However, the details of the high-harmonic spectra strongly vary for different pulses. U_c^g is found to scale linearly with the Fermi velocity v_F, which determines the slope of the Dirac cone. The present results for graphene resemble some of those found for bulk solids in multiband approximations [9,7] and should therefore be useful for understanding the HHG in bulk crystals, in particular the complex interplay between interband and intraband dynamics.

ACKNOWLEDGMENTS

We gratefully acknowledge insightful discussions with Kenichi Ishikawa. Work supported by the Austrian Fonds zur Förderung der wissenschaftlichen Forschung (FWF) through the FWF-SFB 041-ViCom, FWF-SFB 049-NextLite, FWF P-23359-N16 and FWF doctoral college Solids4Fun (W1243). Calculations were performed on the Vienna Scientific Cluster.

[1] A. McPherson, G. Gibson, H. Jara, U. Johann, T. S. Luk, I. A. McIntyre, K. Boyer, and C. K. Rhodes, J. Opt. Soc. Am. B **4**, 595 (1987).
[2] M. Ferray, A. L'Huillier, X. F. Li, L. A. Lompre, G. Mainfray, and C. Manus, J. Phys. B: At., Mol. Opt. Phys. **21**, L31 (1988).
[3] P. B. Corkum, Phys. Rev. Lett. **71**, 1994 (1993).
[4] S. Ghimire, A. D. DiChiara, E. Sistrunk, P. Agostini, and L. F. DiMauro, Nat. Phys. **7**, 138 (2011).
[5] O. Schubert, M. Hohenleutner, F. Langer, B. Urbanek, C. Lange, U. Huttner, D. Golde, T. Meier, M. Kira, S. W. Koch, and R. Huber, Nat. Photonics **8**, 119 (2014).
[6] T. T. Luu, M. Garg, S. Yu. Kruchinin, A. Moulet, M. Th. Hassan, and E. Goulielmakis, Nature (London) **521**, 498 (2015).
[7] D. Golde, T. Meier, and S. W. Koch, Phys. Rev. B **77**, 075330 (2008).
[8] G. Vampa, C. R. McDonald, G. Orlando, D. D. Klug, P. B. Corkum, and T. Brabec, Phys. Rev. Lett. **113**, 073901 (2014).
[9] G. Vampa, C. R. McDonald, G. Orlando, P. B. Corkum, and T. Brabec, Phys. Rev. B **91**, 064302 (2015).
[10] P. G. Hawkins, M. Yu. Ivanov, and V. S. Yakovlev, Phys. Rev. A **91**, 013405 (2015).
[11] S. Ghimire, A. D. DiChiara, E. Sistrunk, G. Ndabashimiye, U. B. Szafruga, A. Mohammad, P. Agostini, L. F. DiMauro, and D. A. Reis, Phys. Rev. A **85**, 043836 (2012).
[12] T. Higuchi, M. I. Stockman, and P. Hommelhoff, Phys. Rev. Lett. **113**, 213901 (2014).
[13] G. Vampa, T. J. Hammond, N. Thiré, B. E. Schmidt, F. Légaré, C. R. McDonald, T. Brabec, and P. B. Corkum, Nature (London) **522**, 462 (2015).
[14] G. Vampa, T. J. Hammond, N. Thiré, B. E. Schmidt, F. Légaré, C. R. McDonald, T. Brabec, D. D. Klug, and P. B. Corkum, Phys. Rev. Lett. **115**, 193603 (2015).
[15] P. Bowlan, E. Martinez-Moreno, K. Reimann, T. Elsaesser, and M. Woerner, Phys. Rev. B **89**, 041408(R) (2014).
[16] M. J. Paul, Y. C. Chang, Z. J. Thompson, A. Stickel, J. Wardini, H. Choi, E. D. Minot, B. Hou, J. A. Nees, T. B. Norris, and Y.-S. Lee, New J. Phys. **15**, 085019 (2013).
[17] A. Y. Bykov, T. V. Murzina, M. G. Rybin, and E. D. Obraztsova, Phys. Rev. B **85**, 121413(R) (2012).

[18] E. Hendry, P. J. Hale, J. Moger, A. K. Savchenko, and S. A. Mikhailov, Phys. Rev. Lett. **105**, 097401 (2010).
[19] J. Maysonnave, S. Huppert, F. Wang, S. Maero, C. Berger, W. de Heer, T. B. Norris, L. A. De Vaulchier, S. Dhillon, J. Tignon, R. Ferreira, and J. Mangeney, Nano Lett. **14**, 5797 (2014).
[20] H. A. Hafez, I. Al-Naib, M. M. Dignam, Y. Sekine, K. Oguri, F. Blanchard, D. G. Cooke, S. Tanaka, F. Komori, H. Hibino, and T. Ozaki, Phys. Rev. B **91**, 035422 (2015).
[21] K. L. Ishikawa, Phys. Rev. B **82**, 201402(R) (2010).
[22] K. L. Ishikawa, New J. Phys. **15**, 055021 (2013).
[23] H. K. Kelardeh, V. Apalkov, and M. I. Stockman, Phys. Rev. B **91**, 045439 (2015).
[24] I. Al-Naib, J. E. Sipe, and M. M. Dignam, Phys. Rev. B **90**, 245423 (2014).
[25] K. S. Virk and J. E. Sipe, Phys. Rev. B **76**, 035213 (2007).
[26] C. Zener. Proc. R. Soc. London, Ser. A **145**, 523 (1934).
[27] L. A. Chizhova, F. Libisch, and J. Burgdörfer, Phys. Rev. B **94**, 075412 (2016).
[28] P. Gibbon, *Short Pulse Laser Interactions With Matter: An Introduction* (Imperial College Press, London, 2005).
[29] M. V. Berry and R. J. Mondragon. Proc. R. Soc. London, Ser. A **412**, 53 (1987).
[30] G. Kaiser, *A Friendly Guide to Wavelets*, Modern Birkhäuser Classics (Birkhäuser, Boston, MA, 2011).
[31] F. Libisch, S. Rotter, and J. Burgdörfer, New J. Phys. **14**, 123006 (2016).
[32] D. C. Elias, R. V. Gorbachev, A. S. Mayorov, S. V. Morozov, A. A. Zhukov, P. Blake, L. A. Ponomarenko, I. V. Grigorieva, K. S. Novoselov, F. Guinea, and A. K. Geim, Nat. Phys. **7**, 701 (2011).
[33] D. M. Basko, Phys. Rev. B **87**, 165437 (2013).
[34] I. Al-Naib, M. Poschmann, and M. M. Dignam, Phys. Rev. B **91**, 205407 (2015).
[35] P. Bowlan, E. Martinez-Moreno, K. Reimann, M. Woerner, and T. Elsaesser, New J. Phys. **16**, 013027 (2014).
[36] J. M. Iglesias, M. J. Martin, E. Pascual, and R. Rengel, J. Phys.: Conf. Ser. **647**, 012003 (2015).